CANONIC SIGNED SPIKE CODING FOR EFFICIENT SPIKING NEURAL NETWORKS

Anonymous authors
Paper under double-blind review

ABSTRACT

Spiking Neural Networks (SNNs) seek to mimic the spiking behavior of biological neurons and are expected to play a key role in the advancement of neural computing and artificial intelligence. The conversion of Artificial Neural Networks (ANNs) to SNNs is the most widely used training method, which ensures that the resulting SNNs perform comparably to ANNs on large-scale datasets. The efficiency of these conversion-based SNNs is often determined by the neural coding schemes. Current schemes typically use spike count or timing for encoding, which is linearly related to ANN activations and increases the required number of time steps. To address this limitation, we propose a novel Canonic Signed Spike (CSS) coding scheme. This method incorporates non-linearity into the encoding process by weighting spikes at each step of neural computation, thereby increasing the information encoded in spikes. We identify the temporal coupling phenomenon arising from weighted spikes and introduce negative spikes along with a Ternary Self-Amplifying (TSA) neuron model to mitigate the issue. A one-step silent period is implemented during neural computation, achieving high accuracy with low latency. We apply the proposed methods to directly convert full-precision ANNs and evaluate performance on CIFAR-10 and ImageNet datasets. Our experimental results demonstrate that the CSS coding scheme effectively compresses time steps for coding and reduces inference latency with minimal conversion loss.

1 INTRODUCTION

Spiking Neural Networks (SNNs), recognized as the third generation of neural network models, are inspired by the biological structure and functionality of the brain (Wang et al., 2020). Unlike traditional Artificial Neural Networks (ANNs), which rely on continuous activation functions, SNNs utilize discrete spiking events. This enables SNNs to capture temporal dynamics and process information in a manner that closely resembles brain activity (Taherkhani et al., 2020). The event-driven nature of SNNs aligns with the brain's energy-efficient computational paradigm, offering potential for more efficient and low-power computing systems (Yamazaki et al., 2022).

The two primary learning algorithms for SNNs are gradient-based optimization and ANN-SNN conversion. Directly training using supervised backpropagation is challenging due to the non-differentiable nature of spike generation (Lee et al., 2020; 2016). The conversion-based method, however, offers a practical approach to overcome this difficulty and has produced the best-performing SNNs (Deng & Gu, 2021; Bu et al., 2022; Ding et al., 2021).

Encoding the ANN activations into spike trains is a prerequisite for successful ANN-SNN conversion. Various coding schemes, such as rate coding and temporal coding, have been proposed to describe neural activity (Guo et al., 2021). Rate coding maps the number of spikes to the corresponding ANN activation (Cao et al., 2015). In contrast, temporal coding focuses on the precise timing or patterns of spikes (Rueckauer & Liu, 2018; Kim et al., 2018; Han & Roy, 2020). For example, Time-to-First-Spike (TTFS) coding maps the the activation value to the time elapsed before the first spike (Stanojevic et al., 2022).

However, both the spike counts in rate coding and the spike timing in TTFS coding are linearly related to the encoded activation. This necessitates a large number of time steps to provide sufficient encoding granularity (Stanojevic et al., 2023; Meng et al., 2022). Recent works have proposed alleviating these problems by quantizing the ANN activations before conversion (Hu et al., 2023;

Bu et al., 2023; Hao et al., 2023). This approach simplifies the encoding process but introduces additional quantizing and training overhead. Our goal is to develop a novel encoding method that can directly convert full-precision ANNs while reducing the number of time steps required.

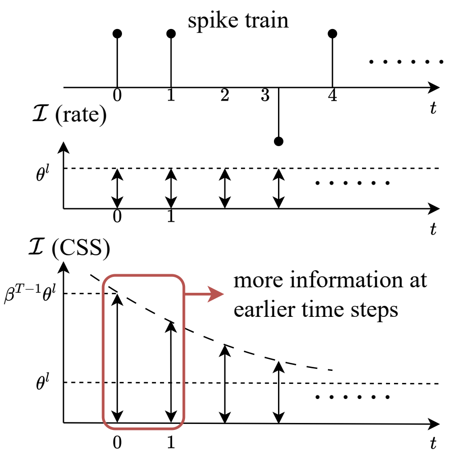

Figure 1: Different interpretations of the same spike sequence. $\mathcal{I}$ denotes the information encoded in a spike. θ^l is the spike amplitude. β is the membrane potential amplification coefficient and T is the total length of the sequence.

In the study of the temporal information dynamics of spikes, Kim et al. (2022) found that after training, information becomes highly concentrated in the first few time steps. This observation led us to hypothesize that the spikes at earlier time steps carry more information and contribute more to the membrane potential. Consequently, by gradually amplifying the membrane potential over time, we increase the influence of earlier spikes. This mechanism essentially assigns exponentially decreasing weights to a spike sequence, with the smallest weight being one (applied to the final spike). This results in a significant enhancement in the encoding capacity of the spike sequence for a given length. Due to this fixed weight pattern during neural computation, we refer to these spikes as canonical.

However, we observed that after weighting, spikes tend to concentrate in later time steps. This phenomenon occurs because earlier spikes now encode larger values, making them less likely to be fired after stimulation. As the spatial depth increases, the spike distribution becomes more biased toward later time steps, leading to significant performance degradation. We refer to this phenomenon as temporal coupling of weighted spikes.

To mitigate this, we introduce negative spikes and lower the firing threshold of neurons to promote earlier spike emission. Neurons are also equipped with a negative spike threshold, allowing them to generate negative spikes that correct excessive firing. This combination results in the Canonic Signed Spike (CSS) coding scheme and the Ternary Self-Amplifying (TSA) neuron model. To better balance the trade-off between coding time steps and inference latency in CSS coding, we introduce a one-step silent period into the TSA neuron, which improves both performance and efficiency of the resulting SNN.

The main contributions of this paper can be summarized as follows:

- By assigning weights to the spikes, we introduce non-linearity into the coding process and compress the time steps to a logarithmic scale. Neurons amplify the membrane potential at each time step, thereby obtaining more information from the preceding spikes.
- We find that weighted spikes are prone to temporal coupling during neural computation, presenting the biggest challenge when incorporating non-linearity in spike coding. We analyze the underlying reasons and introduces negative spikes along with the TSA neuron model to address this issue.
- We demonstrate the effectiveness of the CSS coding scheme on the CIFAR-10 and ImageNet datasets. The results show that the proposed method effectively reduces both the required coding time steps and inference latency. Additionally, the CSS coding scheme offers energy efficiency advantages over both rate coding and temporal coding.

2 RELATED WORK

Currently, the mainstream coding schemes in converted SNNs are rate coding and TTFS coding. Rate coding represents different activities with the number of spikes emitted within a specific time window. Early research efforts focused on reducing conversion loss, leading to methods such as weight normalization (Diehl et al., 2015), threshold rescaling (Sengupta et al., 2019), and soft-reset neuron models (Han et al., 2020). More recent work has shifted towards reducing the number of time steps by optimizing neuron parameters. Meng et al. (2022) introduced the Threshold Tuning and Residual Block Restructuring (TTRBR) method to minimize conversion error in ResNet architectures with fewer time steps. Bu et al. (2022) proposed optimizing the initial membrane potential to reduce conversion loss when using a small number of time steps.

Despite these optimizations, deep networks or large datasets still require hundreds of time steps to achieve satisfactory results. To address this, recent works in rate coding have explored quantizing the ANNs before conversion (Hao et al., 2023; Bu et al., 2023; Hu et al., 2023). This approach directly reduces the number of activations that need to be mapped, providing an alternative way to minimize time steps. Notably, this approach is complementary to ours. The proposed encoding scheme can also convert quantized ANNs and further reduce the required number of time steps.

Due to the functional similarity to the biological neural network, SNNs are highly compatible with temporal coding. Rueckauer & Liu (2018) were the first to attempt converting an ANN to a TTFS-based SNN. While this coding method significantly increased sparsity by limiting each neuron to fire at most one spike, they observed large conversion errors, even on MNIST dataset. Stanojevic et al. (2022) demonstrated that an exact mapping from ANN to TTFS-based SNN is feasible but needs hundreds of time steps for accurate encoding. Yang et al. (2023) proposed a TTFS-based conversion algorithm with dynamic neuron threshold and weight regularization. They completed the conversion with 50 time steps per layer. Despite the reduction in the number of time steps per layer, TTFS coding still suffered from high output latency in deep networks for its layerwise processing manner. Han & Roy (2020) introduced the Temporal-Switch-Coding (TSC) scheme, where each input pixel is represented by two spikes, and the time interval between them encodes pixel intensity. However, as this time interval remains linearly related to activation, the issue of long latency persists.

Some recent works have also incorporated non-linearity into the coding process. Stöckl & Maass (2021) and Rueckauer & Liu (2021) used spikes to encode the ”1”s in the binary representations of ANN activations. However, both works did not address the temporal coupling issue caused by weighted spikes. Instead, they adopted an approach similar to TTFS coding, where neurons must wait for the arrival of all input spikes before firing. In contrast, our approach facilitates the greatest extent of synchronous neural computation, thereby reducing both the coding time steps and output latency.

3 PRELIMINARIES

3.1 SPIKING NEURONS

Spiking neurons communicate through spike trains and are interconnected via synaptic weights. Each incoming spike contributes to the postsynaptic neuron's membrane potential, and a spike is generated when the potential reaches a predefined threshold. Generally, a spike sequence $S_i^l[t]$ in the SNN can be expressed as follows:

$$S_i^l[t] = \sum_{t_i^{l,f} \in \mathbb{F}_i^l} \theta^l \delta[t - t_i^{l,f}] \tag{1}$$

where i is the neuron index, l is the layer index, θ^l is the spike amplitude, $\delta[\cdot]$ denotes an unit impulse[1], f is the spike index, and $\mathbb{F}_i^l$ denotes a set of spike times which satisfies the firing condition:

$$t_i^{l,f} : o_i^l[t_i^{l,f}] \geq \theta^l \tag{2}$$

where $o_i^l[t]$ denotes the membrane potential before firing a spike. Conversion-based works often employ soft-reset IF neuron model, where the membrane potential is subtracted by an amount equal to the spike amplitude for reset. Specifically, its dynamics can be expressed as follows:

$$u_i^l[t] = u_i^l[t-1] + z_i^l[t] - S_i^l[t] \tag{3}$$

where $u_i^l[t]$ denotes the membrane potential after firing a spike and $z_i^l[t]$ denotes the integrated inputs:

$$z_i^l[t] = \sum_j w_{ij}^l S_j^{l-1}[t] + b_i^l \tag{4}$$

where w_{ij}^l is the synaptic weight and b_i^l is the bias. For clarity, definitions of the common symbols are provided in Table 1.

---

[1] $\delta[t]$ takes the value 1 at $t = 0$, and 0 otherwise

Table 1: Common symbols in this paper.

Symbol	**Definition**	**Symbol**	**Definition**
l	Layer index	β	Amplification factor
i, j	Neuron index	w_{ij}^l	SNN weight
$S_i^l[t]$	Spike sequence	$\hat{w}_{ij}^l$	ANN weight
$o_i^l[t]$	Membrane potential before firing	b_i^l	SNN bias
$u_i^l[t]$	Membrane potential after firing	$\hat{b}_i^l$	ANN bias
$z_i^l[t]$	Integrated inputs (PSP)[1]	T	Time steps for coding
θ^l	Spike amplitude	$\tilde{\theta}^l$	Initial spike amplitude

[1] Postsynaptic potential

3.2 ANN-SNN CONVERSION

The ANN-SNN conversion typically involves the following two key steps: 1) selecting an appropriate encoding method to represent ANN activations as spike trains, and 2) adopting a suitable neuron model that ensures the generated spike trains accurately encode the outputs of the corresponding ANN neurons. Note that this process results from the joint effect of the encoding scheme and the neuron model.

The most widely used and State-Of-The-Art (SOTA) approaches employ (signed) soft-reset IF neurons and interprets their output through spike rates (i.e. rate coding). Let T denote the number of time steps, with the initial condition $u_i^l[0] = 0$, we can iteratively update the membrane potential using Eq. (3) until $t = T$. Then substitute $z_i^l[t]$ with Eq. (4), and we can write:

$$\frac{\sum_{t=1}^{T} S_i^l[t]}{T} = \sum_j w_{ij}^l \frac{\sum_{t=1}^{T} S_j^{l-1}[t]}{T} + \sum_{t=1}^{T} \frac{b_i^l}{T} - \frac{u_i^l[T]}{T} \tag{5}$$

See Appendix A.1 for a detailed derivation. Note that both sides of the equation are divided by T to better highlight the interpretation of $\sum_{t=1}^{T} S_i^l[t]/T$ as a "rate". It defines the relationship between neuron's input rate and output rate and can be directly related to the forward pass in a ReLU-activated ANN:

$$a_i^l = \max\left(\sum_j \hat{w}_{ij}^l a_j^{l-1} + \hat{b}_i^l, 0\right) \tag{6}$$

where a_i^l denotes the ANN activation, $\hat{w}_{ij}^l$ and $\hat{b}_i^l$ denote the weight and bias, respectively. Note that in Eq. (5) we have: 1) $\sum S[t]/T > 0$, and 2) $u_i^l[T]/T$ becomes negligible as T increases. These observations suggest that mapping ANN activations to SNN spike rates can be achieved by simply using the scaled ANN weights[2] and bias.

However, with fewer time steps, the spike rate $\sum S_i^l[t]/T$ can only encode a limited number of activations, while the perturbation introduced by $u_i^l[T]/T$ increases. These factors together result in a rapid increase in conversion loss. This issue is inherent in any encoding scheme that relies on quantities linearly related to the time steps. Therefore, our goal is to incorporate nonlinearity into the encoding process to enhance the expressiveness of spike trains.

4 METHODS

4.1 ASSIGNING WEIGHTS TO SPIKES

We begin by introducing an amplification factor $\beta > 1$ into the soft-reset IF model:

$$u_i^l[t] = \beta u_i^l[t-1] + z_i^l[t] - S_i^l[t] \tag{7}$$

---

[2] The spile amplitude θ^l is finally normalized to 1 for simplicity of implementation, which is achieved by absorbing it into the synaptic weights. Consequently, the ANN weights still need to be scaled by a certain factor. Note that θ^l is typically determined based on the number of time steps and the range of ANN activations in layer l.

Following the same derivation as in Eq. (5), we can write:

$$u_i^l[T] = \sum_j w_{ij}^l \sum_{t=1}^{T} \beta^{T-t} S_j^{l-1}[t] + \sum_{t=1}^{T} \beta^{T-t} b_i^l - \sum_{t=1}^{T} \beta^{T-t} S_i^l[t] \tag{8}$$

The detailed derivation can be found in Appendix A.1. As expected, the input at time $t_i^{l,f}$ raises the membrane potential by $\theta^l \beta^{T-t_i^{l,f}}$. As shown in Fig. 1, for a sequence of length T, this enables the use of $\sum_{t=1}^{T} \beta^{T-t} S_i^l[t]$ rather than $\sum_{t=1}^{T} S_i^l[t]$ to map the ANN activation. Note the spike at time T still encodes θ^l, which is the minimum value a spike can represent and determines the granularity of encoding.

Definition 1. Let v denote the target value. The encoding is considered accurate, denoted as $S_i^l[t] \sim v$, as long as $\left|\sum_{t=1}^{T} \beta^{T-t} S_i^l[t] - v\right| < \theta^l$.

We allow a discrepancy of one spike amplitude between the target and encoded value, which can be considered as a quantization error due to the finite number of time steps. According to Eq. (8), our method can theoretically encode the same number of activations as linear encoding method while log-compressing the number of required time steps. Meanwhile, Eq. (8) serves as the core equation for ANN-SNN conversion. We can rewrite it as follows:

$$\sum_{t=1}^{T} \beta^{T-t} S_i^l[t] = \sum_j w_{ij}^l \sum_{t=1}^{T} \beta^{T-t} S_j^{l-1}[t] + \sum_{t=1}^{T} \beta^{T-t} b_i^l - u_i^l[T]$$

By comparing the above equation with Eq. (6), and noting that $\sum_t \beta^{T-t} S_i^l[t] \geq 0$, we can conclude:

Observation 1. Let $S_j^{l-1}[t] \sim a_j^{l-1}$, and set $w_{ij}^l = \hat{w}_{ij}^l$ and $b_i^l = \hat{b}_i^l / \sum_t \beta^{T-t}$, respectively. To reduce encoding errors in layer l, the residual membrane potential $u_i^l[T]$ should be minimized.

Building on this insight, we now identify the factors influencing $u_i^l[T]$, as formalized in the following theorem:

Theorem 1. *Making $u_i^l[T] < \epsilon$ is equivalent to satisfying the following equation:*

$$\begin{aligned}&\forall t_0 \in \{1, 2, \cdots, T\},\\ &\beta^{T-t_0+1} u_i^l[t_0 - 1] + \sum_j w_{ij}^l \sum_{t=t_0}^{T} \beta^{T-t} S_j^{l-1}[t] + \sum_{t=t_0}^{T} \beta^{T-t} b_i^l < \epsilon + \sum_{t=t_0}^{T} \theta^l \beta^{T-t}\end{aligned} \tag{9}$$

The second term on the right-hand side of Eq. (9) represents the maximum value a spike train after t_0 can encode. This imposes constraints on both the subsequent input and the membrane potential carried over from the preceding step (the left-hand side of the equation). Theorem 1 provides the mathematical foundation for the next section, with its detailed derivation available in Appendix A.2.

4.2 INCORPORATING NEGATIVE SPIKES

Rueckauer et al. (2017) reported that large activation values in ANNs are rare, with most values concentrated within a smaller range. This suggests that when mapped to weighted spike trains, the majority of spikes will occur in the later time steps (as these spikes encode smaller values). As a consequence, Eq. (9) becomes difficult to satisfy as t_0 approaches T: the left-hand side contains a large amount of input, while the right-hand side provides limited encoding capacity. This mismatch ultimately results in an increase in $u_i^l[T]$, leading to a further shift in the spike distribution.

To illustrate this more clearly, we have plotted the spike distribution in the first and last layers of VGG-16 (in red) in Fig. 2, alongside the distribution of the average residual membrane potential across all neurons. As shown, the spike distribution in the last layer shifts significantly toward later time steps compared to the first layer, a phenomenon we refer to as the temporal coupling of weighted spikes. Additionally, the residual membrane potential exhibits a distribution resembling random noise, and our experimental results indicate that this leads to nearly random classification performance. Therefore, a new neuron model is needed to enable effective computation with weighted spikes.

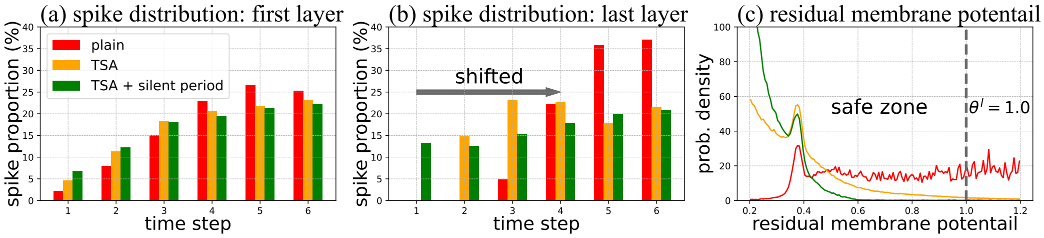

Figure 2: (a) Spike distribution in the first layer of VGG-16. (b) Spike distribution in the last layer of VGG-16. (c) Average residual membrane potential across all neurons in VGG-16. The red data corresponds to the self-amplifying IF neuron model, the orange data corresponds to the TSA model, and the green data further incorporates a one-step silent period.

Algorithm 1: The forward method of TSA

```
Input: input $X$ of shape [BT, C, H, W], length of silent period $L$, spike amplitude $\theta$
Output: output spike train $S$ of shape [BT, C, H, W]
reshape and then pad $X$ with zeros to shape [(T+L), B, C, H, W];
membrane potential $M \leftarrow$ zeros_like $(X[0])$, threshold $v \leftarrow \frac{1}{2}\theta\beta^L$;
for $0 \leq i \leq L$ do
    $M \leftarrow \beta M + X[i]$;                                  /* silent period */
end
for $i = 0$ to $T - 1$ do
    $M \leftarrow \beta M + X[i + L]$;                              /* accumulate input */
    $S[i] \leftarrow (M \geq v)$.float() $-$ $(M \leq -v)$.float() ;   /* fire ternary spikes */
    $M \leftarrow M - 2v \times S[i]$;                              /* over firing & soft reset */
end
```

4.2.1 TERNARY SELF-AMPLIFYING NEURON MODEL

Based on the above analysis, our approach begins by encouraging spikes to be generated as early as possible. The key idea is to lower the firing threshold and incorporate negative spikes into the encoding scheme to correct the excess information caused by over-spiking.

We set the positive firing threshold to $\frac{1}{2}\theta^l$ and introduce a negative threshold of $-\frac{1}{2}\theta^l$ into the neuron model, which triggers a negative spike when $o_i^l[t]$ falls below it. Notably, on the left side of Eq. (9), this adjustment not only shifts the input spikes to earlier time steps, but also reduces $u_i^l[t_0 - 1]$. The coefficient $\frac{1}{2}$ is selected to confine both positive and negative membrane potential within a narrow and balanced range. Given the above characteristics, we designate the coding method as the CSS coding scheme and the neuron model as the TSA neuron.

Next, we establish the connection between the ANN and SNN using the proposed methods. Based on Observation 1, we present the following theorem:

Theorem 2. *Let $S_j^{l-1}[t] \sim a_j^{l-1}$, $w_{ij}^l = \hat{w}_{ij}^l$, and $b_i^l = {\hat{b}_i^l}/{\sum_t \beta^{T-t}}$. Then $S_i^l[t] \sim a_i^l$, provided that $\left|u_i^l[T]\right| < \theta^l$.*

Note $S_i^l[t]$ can now represent negative activations with negative spikes. To handle this, we constrain the absolute value of $u_i^l[T]$ and apply additional logic to zero out sequences that encode negative values (a ReLU counterpart). The above theorem supposes that the input has been encoded and then provides the method for output encoding. Next, we give the method to encode the network input:

Theorem 3. *Let the input pixel value be a_i^0 and $\beta \leq 2$. By Initializing the membrane potential $u_i^0[0]$ with ${a_i^0}/{\beta^T}$, the resulting spike train $S_i^0[t] \sim a_i^0$ with T steps.*

The proofs of the above two theorems can be found in Appendix A.2. By encoding input with Theorem 3 and constraining $u_i^l[T]$ of each hidden layer within the requirements of Theorem 2, an ANN is then converted to a CSS-coded SNN.

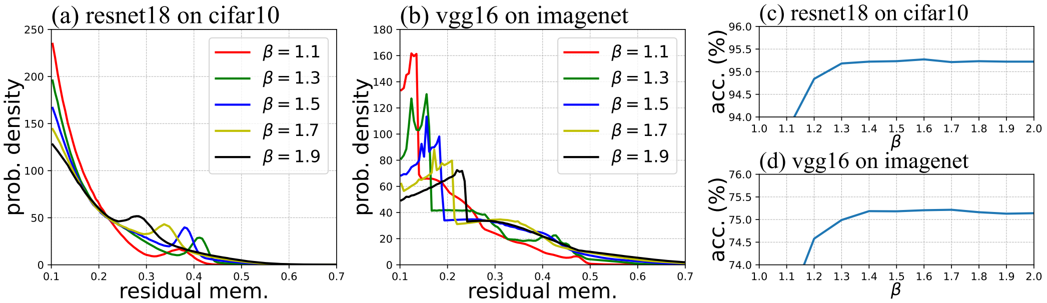

Figure 3: Impact of β on residual membrane potential and accuracy. Membrane potentials are normalized by the spike amplitude. (a) and (b) show the residual membrane potential distributions under different β. (c) and (d) show accuracy variations corresponding to different β.

4.2.2 ONE-STEP SILENT PERIOD

Although the TSA neuron effectively controls $u_i^l[T]$ within an acceptable range, the results in Fig. 2 (orange) demonstrate that temporal coupling persists. Inspired by the layerwise processing manner in TTFS coding (Stanojevic et al., 2022), we incorporate a one-step silent period into the TSA neuron model. During this period, neurons integrate input and perform stepwise weighting but are prohibited from firing. This one-step output delay introduces a new term, $\theta^l \beta^{T-t_0-1}$ (i.e. spike from $t = t_0 - 1$), to the right-hand side of Eq. (9), making it easier to minimize $u_i^l[T]$.

Since the input information is amplified by β after the silent period, the firing threshold is adjusted to $\frac{\beta}{2}\theta^l$ accordingly. Similarly, the membrane potential is reduced by $\beta\theta^l$ for reset. In Algorithm 1, we provide pseudo code for the forward propagation process of TSA neurons. The mathematical description of the TSA neuron model can be found in Appendix A.5.

The silent period method assigns distinct computation time windows to TSAs at different depths, aligning with the temporal shift of the input spike distribution. This partially sacrifices synchronous processing at each time step, leading to increased output latency. For an L-layer network, the output layer will start to fire spikes only after L steps. However, with each layer operating in a pipelined manner, the efficiency and accuracy gain outweighs the drawback of the increased latency. In Appendix A.4, we set up an ablation study to evaluate the effectiveness of this trade-off.

5 EXPERIMENTS

5.1 EXPERIMENTAL SETUP

Determination of Spike Amplitude. We use a strategy similar to rate coding (Rueckauer et al., 2017) to derive a suitable θ^l: after observing the ANN activations over a portion of the training set, we calculate the 99.99th percentile p^l of the activation distribution, and then set θ^l to ${}^{p^l}/_{\sum_t \beta^{T-t}}$.

This setting ensures that the vast majority of the activations remain below the maximum encodable value, $\sum_t \theta^l \beta^{T-t}$, and increases the network's robustness to outlier activations. For ImageNet, we further fine-tune the spike amplitude; additional details on this process can be found in Appendix A.3.

Choice of the Amplification Factor. To investigate the impact of β, we conducted experiments using ResNet-18 on CIFAR-10 and VGG-16 on ImageNet. We plotted the distribution of the residual membrane potential for different values of β (which serves as an indicator of temporal coupling) and provided the corresponding accuracy curves in Fig. 3

As shown, accuracy generally increases and then decreases as β varies. As β increases, the weight difference between spikes grows, causing input spikes to cluster at later time steps and increasing the likelihood of temporal coupling. Conversely, a decrease in β requires a larger θ^l to provide the same encoding capacity, which in turn leads to a higher quantization error. Notably, for $\beta \geq 1.4$, the network exhibits relatively stable performance, with the accuracy difference becoming less pronounced as β increases.

Table 2: Coding time steps and inference latency under different neural coding schemes, evaluated on CIFAR-10 and ImageNet datasets.

	Methods	**Architecture**	**ANN Accuracy**	**Coding Scheme**	**Coding Time Steps**	**Inference Latency**	**SNN Accuracy**
CIFAR-10	FS-conversion (Stöckl & Maass, 2021)	ResNet-20	91.58%	FS	10	200	91.45%
	TTRBR (Meng et al., 2022)	ResNet-18	95.27%	rate	128	128	95.18%
	TSC (Han & Roy, 2020)	VGG-16	93.63%	TSC	512	512	93.57%
	LC-TTFS (Yang et al., 2023)	VGG-16	92.79%	TTFS	50	800	92.72%
	Exact mapping (Stanojevic et al., 2023)	VGG-16	93.68%	TTFS	64	1024	93.64%
	Calibration (Li et al., 2021)	VGG-16	95.72%	rate	128	128	95.65%
	OPI (Bu et al., 2022)	VGG-16	94.57%	rate	128	128	94.50%
	CSS-SNN	ResNet-20	92.10%	CSS	12	32	92.06%
		ResNet-18	95.24%		12	30	95.30%
		VGG-16	95.89%		10	26	95.88%
ImageNet	OPI (Bu et al., 2022)	VGG-16	74.85%	rate	256	256	74.62%
	TSC (Han & Roy, 2020)	VGG-16	73.49%	TSC	1024	1024	73.33%
	RMP-SNN Han et al. (2020)	VGG-16	73.49%	rate	2048	2048	72.78%
	Calibration (Li et al., 2021)	VGG-16	75.36%	rate	256	256	74.23%
	TSC (Han & Roy, 2020)	ResNet-34	70.64%	TSC	4096	4096	69.93%
	CalibrationLi et al. (2021)	ResNet-34	75.66%	rate	256	256	74.61%
	FS-conversion (Stöckl & Maass, 2021)	ResNet-50	75.22%	FS	10	500	75.10%
	TTRBR (Meng et al., 2022)	ResNet-50	76.02%	rate	512	512	75.04%
	CSS-SNN	VGG-16	75.34%	CSS	12	28	75.24%
		ResNet-34	76.42%		14	48	76.22%
		ResNet-50	80.85%		16	66	80.10%

Based on these observations, we set β to 1.5 for two key reasons: it lies near the midpoint of the range, and more importantly, it allows for membrane potential amplification through simple shifting and addition operations, which is energy-efficient and facilitates future hardware implementation.

5.2 OVERALL PERFORMANCE

In Table 2, we compared the time steps and inference latency under different coding schemes, which reflect the throughput and latency of the network, respectively. Note all SNNs are converted from full-precision ANNs to ensure a fair comparison. Furthermore, the accuracy of the ANNs utilized in each work is also provided.

Reduction in Coding Time Steps. The coding time steps refer to the number of time steps required to encode the activations into a spike train. This metric indicates how well the encoding scheme can represent information within a given time frame and reflects the efficiency of the method.

For simpler classification tasks such as CIFAR-10, CSS coding scheme demonstrated nearly lossless conversion with a significant reduction in the number of required time steps. Compared to linear coding schemes like rate coding, CSS reduces time steps by more than tenfold for both VGG-16 and ResNet-18, while simultaneously reducing the conversion loss. While the FS coding scheme also applied weighted spikes and required fewer time steps for ResNet-20, it experienced greater conversion loss compared to our method. On the more complex ImageNet dataset, the higher precision demands for encoding further highlighted the benefits of spike weighting. For example, Li et al. (2021) reported a conversion error exceeding 1% on ResNet-34 with 256 time steps, whereas our method achieved only 0.2% conversion loss with just 14 time steps. FS-coding achieved smaller conversion loss for ResNet-50 with fewer time steps; however, this came at the cost of a latency eight times greater than that of ours.

Reduction in Inference Latency. Inference latency refers to the time elapsed from the beginning of input encoding to the receipt of the classification result, and is also measured in time steps. It indicates how efficiently the encoding scheme transmits information through neural computation across the network layers.

In CSS coding scheme, each layer of TSA neurons incorporates a one-step silent period, making the inference latency equal to the sum of layer counts and coding time steps. In contrast, both TTFS coding and FS coding require each layer to wait for the arrival of all inputs. While this approach facilitates lossless conversion, it completely sacrifices the synchronous processing capability of SNNs, leading to increased output latency (i.e. the product of layer counts and coding time steps). For in-

Table 3: Performance of Fast-SNN, Offset, and CSS on ImageNet after converting 3-bit VGG-16. The results for both Fast-SNN (Hu et al., 2023) and Offset (Hao et al., 2023) are self-implemented using their publicly available repositories, ensuring identical pre-conversion ANN accuracy.

Methods	**T=1**	**T=2**	**T=3**	**T=4**	**T=5**	**T=6**	**T=7**	**T=8**
Offset (rate)	**64.90%** (129 steps)	**70.85%** (130 steps)	72.06% (131 steps)	72.53% (132 steps)	72.79% (133 steps)	72.92% (134 steps)	73.05% (135 steps)	73.01% (136 steps)
Fast-SNN (rate)	3.19% (1 step)	52.74% (2 steps)	68.13% (3 steps)	71.26% (4 steps)	72.21% (5 steps)	72.64% (6 steps)	72.87% (7 steps)	72.97% (8 steps)
CSS	2.87% (17 steps)	68.53% (18 steps)	**72.81%** (19 steps)	**73.25%** (20 steps)	**73.23%** (21 steps)	**73.24%** (22 steps)	**73.23%** (23 steps)	**73.24%** (24 steps)

stance, in the CIFAR-10 classification task, the inference latency reported by Stanojevic et al. (2023) on VGG-16 is about 40 times that of our method. FS coding, as a nonlinear encoding scheme, performs well in both coding steps and conversion loss, but its output latency remains a major weakness; on ResNet-20, its latency exceeds that of CSS by over six times. Rate coding enables synchronous processing, but its inference latency is constrained by the large number of coding time steps. In the ImageNet classification task, for example, rate-coded ResNet-34 has a latency five times greater than our method.

5.3 COMBINATION WITH QUANTIZED ANNS

SOTA performance SNNs (Hu et al., 2023; Hao et al., 2023) are typically achieved by converting quantized ANNs, while still utilizing rate coding. To ensure that only the encoding scheme varies, we convert ANNs with identical precision. Experiments were conducted using a 3-bit VGG-16 on ImageNet, with the results presented in Table 3. T represents the number of coding time steps, and the inference latency is given in round brackets. Note we set β to 2 for quantized networks as this ensures the encoded values align well with the quantized activations. Additionally, the membrane potential amplification can be achieved using only shifting operations.

Compared to Fast-SNN, our method achieves ANN-level accuracy with fewer time steps by leveraging weighted spikes. The IF neurons in Fast-SNN, which do not require a silent period, naturally exhibit better output latency. In contrast, Offset improves accuracy with minimal time steps by calibrating the initial membrane potential of neurons. However, this comes at the cost of significantly increased output latency, as each layer requires ρ time steps (with $\rho = 8$ for ImageNet, consistent with the original paper) to determine how to calibrate the initial membrane potential. This per-layer latency accumulates across the network, similarly to the silent period in our approach.

Theoretically, the benefits of our method become more pronounced with higher ANN bit precision (as shown in Table 2), as spike weighting exponentially reduces the number of time steps. While rate coding also perform well with reduced time steps, they rely heavily on low-bit quantization. This introduces overhead in training and often sacrifices accuracy. CSS coding scheme provides an alternative approach to achieving low time steps in SNNs without relying on aggressive quantization. Furthermore, our method can be seamlessly combined with quantized ANNs, enabling the development of higher-performance SNNs.

5.4 ENERGY CONSUMPTION ANALYSIS

In this section, we estimate the energy consumption of our methods[3], with the results summarized in Table 4. The results show that the CSS-coded SNNs achieve at least a fivefold reduction in energy consumption compared to the original ANN. TTFS (Stanojevic et al., 2023) coding demonstrates extremely low energy consumption due to its theoretical minimum spike count. While our method does not inherently exhibit sparse characteristics, the reduction in coding time steps mitigates this disadvantage. By further compressing the number of time steps, our approach achieves a 10% reduction in energy consumption compared to TTFS. Additionally, we include Fast-SNN (Hu et al., 2023) as a strong baseline for (signed) rate coding. The results show that our method outperforms

---

[3] Energy consumption measurements were performed using the code from `https://github.com/iCGY96/syops-counter`

Table 4: Energy consumption of SNNs on CIFAR-10.

Methods	**Arch.**	**Accuracy**	**T**	**Latency**	SyOPs (ACs)	MACs	Energy Consumption
ANN	VGG-11	93.82%	N/A	N/A	0	153.2M	0.7047mJ
CSS	VGG-11	93.78%	8	19	0	132.4M	0.1191mJ
ANN	VGG-16	95.88%	N/A	N/A	0	313.88M	1.4438mJ
TTFS*	VGG-16	93.53%	64	1024	120.53M	0	0.1085mJ
CSS	VGG-16	95.84%	8	24	308.35M	0	0.2775mJ
CSS†	VGG-16	95.14%	2	18	102.19M	0	0.0920mJ
ANN	ResNet-18	95.25%	N/A	N/A	0	2.22G	10.21mJ
rate (Fast-SNN)†	ResNet-18	95.42%	7	7	1.02G	12.42M	0.9751mJ
rate (Faset-SNN)†	ResNet-18	95.23%	6	6	878.3M	10.65M	0.8395mJ
CSS†	ResNet-18	95.31%	3	21	730.65M	1.84M	0.6660mJ
CSS†	ResNet-18	95.24%	2	20	489.93M	1.91M	0.4497mJ

† The results from converting quantized ANNs.

* Stanojevic et al. (2023) reported an average spike rate of 38% per neuron on VGG-16, which we used to calculate the SyOPs and estimate the energy consumption.

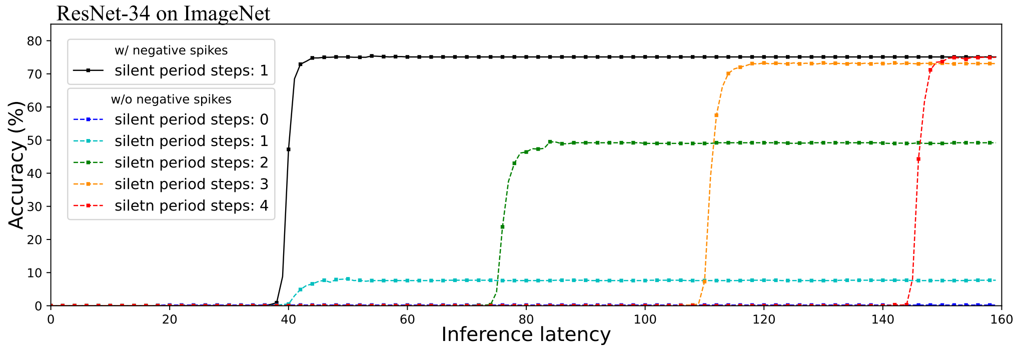

Figure 4: Inference latency with and without negative spikes. The solid line represents the results with negative spikes, while the dashed line indicates the results without negative spikes. The lines of different colors correspond to different lengths of the silent period as shown in the legend.

Fast-SNN with more than a 30% reduction in energy consumption, while maintaining comparable accuracy.

5.5 THE ROLE OF NEGTIVE SPIKES

In this section, we validate the role of negative spikes in achieving low-latency nonlinear encoding through an ablation study. Experiments were conducted using ResNet-34 on ImageNet, where we gradually increased the silent period length from zero, in the absence of negative spikes. The results, shown in Fig. 4, reveal that a silent period of at least four steps is required to match the performance gains introduced by negative spikes. This results in a nearly 100-step increase in inference latency. The introduction of negative spikes and TSA neurons in the CSS coding scheme is crucial for breaking temporal coupling, distinguishing our approach from other coding schemes that use weighted spikes (Rueckauer & Liu, 2021; Stöckl & Maass, 2021; Kim et al., 2018).

6 CONCLUSION AND DISCUSSION

In this work, we compress the coding time steps by assigning weights to spikes, enabling each spike to carry more information. We also introduce negative spikes to break temporal coupling, effectively reducing inference latency. The resulting CSS encoding scheme enhances the throughput, inference speed and energy efficiency of converted SNNs, while minimizing conversion loss.

REFERENCES

Tong Bu, Jianhao Ding, Zhaofei Yu, and Tiejun Huang. Optimized potential initialization for low-latency spiking neural networks, 2022.

Tong Bu, Wei Fang, Jianhao Ding, PengLin Dai, Zhaofei Yu, and Tiejun Huang. Optimal ann-snn conversion for high-accuracy and ultra-low-latency spiking neural networks, 2023.

Yongqiang Cao, Yang Chen, and Deepak Khosla. Spiking deep convolutional neural networks for energy-efficient object recognition. *International Journal of Computer Vision*, 113(1):54–66, May 2015. ISSN 1573-1405. doi: 10.1007/s11263-014-0788-3. URL `https://doi.org/10.1007/s11263-014-0788-3`.

Shikuang Deng and Shi Gu. Optimal conversion of conventional artificial neural networks to spiking neural networks, 2021.

Peter U. Diehl, Daniel Neil, Jonathan Binas, Matthew Cook, Shih-Chii Liu, and Michael Pfeiffer. Fast-classifying, high-accuracy spiking deep networks through weight and threshold balancing. In *2015 International Joint Conference on Neural Networks (IJCNN)*, pp. 1–8, 2015. doi: 10.1109/IJCNN.2015.7280696.

Jianhao Ding, Zhaofei Yu, Yonghong Tian, and Tiejun Huang. Optimal ann-snn conversion for fast and accurate inference in deep spiking neural networks, 2021.

Wenzhe Guo, Mohammed E. Fouda, Ahmed M. Eltawil, and Khaled Nabil Salama. Neural coding in spiking neural networks: A comparative study for robust neuromorphic systems. *Frontiers in Neuroscience*, 15, 2021. ISSN 1662-453X. doi: 10.3389/fnins.2021.638474. URL `https://www.frontiersin.org/journals/neuroscience/articles/10.3389/fnins.2021.638474`.

Bing Han and Kaushik Roy. Deep spiking neural network: Energy efficiency through time based coding. In Andrea Vedaldi, Horst Bischof, Thomas Brox, and Jan-Michael Frahm (eds.), *Computer Vision – ECCV 2020*, pp. 388–404, Cham, 2020. Springer International Publishing.

Bing Han, Gopalakrishnan Srinivasan, and Kaushik Roy. Rmp-snn: Residual membrane potential neuron for enabling deeper high-accuracy and low-latency spiking neural network, 2020.

Zecheng Hao, Jianhao Ding, Tong Bu, Tiejun Huang, and Zhaofei Yu. Bridging the gap between anns and snns by calibrating offset spikes, 2023.

Yangfan Hu, Qian Zheng, Xudong Jiang, and Gang Pan. Fast-snn: Fast spiking neural network by converting quantized ann. *IEEE Transactions on Pattern Analysis and Machine Intelligence*, 45 (12):14546–14562, 2023. doi: 10.1109/TPAMI.2023.3275769.

Jaehyun Kim, Heesu Kim, Subin Huh, Jinho Lee, and Kiyoung Choi. Deep neural networks with weighted spikes. *Neurocomputing*, 311:373–386, 2018. ISSN 0925-2312. doi: https://doi.org/10.1016/j.neucom.2018.05.087. URL `https://www.sciencedirect.com/science/article/pii/S0925231218306726`.

Youngeun Kim, Yuhang Li, Hyoungseob Park, Yeshwanth Venkatesha, Anna Hambitzer, and Priyadarshini Panda. Exploring temporal information dynamics in spiking neural networks, 2022.

Chankyu Lee, Syed Shakib Sarwar, Priyadarshini Panda, Gopalakrishnan Srinivasan, and Kaushik Roy. Enabling spike-based backpropagation for training deep neural network architectures. *Frontiers in Neuroscience*, 14, February 2020. ISSN 1662-453X. doi: 10.3389/fnins.2020.00119. URL `http://dx.doi.org/10.3389/fnins.2020.00119`.

Jun Haeng Lee, Tobi Delbruck, and Michael Pfeiffer. Training deep spiking neural networks using backpropagation, 2016. URL `https://arxiv.org/abs/1608.08782`.

Yuhang Li, Shikuang Deng, Xin Dong, Ruihao Gong, and Shi Gu. A free lunch from ann: Towards efficient, accurate spiking neural networks calibration, 2021.

Qingyan Meng, Shen Yan, Mingqing Xiao, Yisen Wang, Zhouchen Lin, and Zhi-Quan Luo. Training much deeper spiking neural networks with a small number of time-steps. *Neural Networks*, 153:254–268, 2022. ISSN 0893-6080. doi: https://doi.org/10.1016/j.neunet.2022.06.001. URL `https://www.sciencedirect.com/science/article/pii/S0893608022002064`.

Bodo Rueckauer and Shih-Chii Liu. Conversion of analog to spiking neural networks using sparse temporal coding. In *2018 IEEE International Symposium on Circuits and Systems (ISCAS)*, pp. 1–5, 2018. doi: 10.1109/ISCAS.2018.8351295.

Bodo Rueckauer and Shih-Chii Liu. Temporal pattern coding in deep spiking neural networks. In *2021 International Joint Conference on Neural Networks (IJCNN)*, pp. 1–8, 2021. doi: 10.1109/IJCNN52387.2021.9533837.

Bodo Rueckauer, Iulia-Alexandra Lungu, Yuhuang Hu, Michael Pfeiffer, and Shih-Chii Liu. Conversion of continuous-valued deep networks to efficient event-driven networks for image classification. *Frontiers in Neuroscience*, 11, 2017. ISSN 1662-453X. doi: 10.3389/fnins.2017.00682.

Abhronil Sengupta, Yuting Ye, Robert Wang, Chiao Liu, and Kaushik Roy. Going deeper in spiking neural networks: Vgg and residual architectures, 2019. URL `https://arxiv.org/abs/1802.02627`.

Ana Stanojevic, Stanisław Woźniak, Guillaume Bellec, Giovanni Cherubini, Angeliki Pantazi, and Wulfram Gerstner. An exact mapping from relu networks to spiking neural networks, 2022. URL `https://arxiv.org/abs/2212.12522`.

Ana Stanojevic, Stanisław Woźniak, Guillaume Bellec, Giovanni Cherubini, Angeliki Pantazi, and Wulfram Gerstner. High-performance deep spiking neural networks with 0.3 spikes per neuron, 2023. URL `https://arxiv.org/abs/2306.08744`.

Christoph Stöckl and Wolfgang Maass. Optimized spiking neurons classify images with high accuracy through temporal coding with two spikes, 2021. URL `https://arxiv.org/abs/2002.00860`.

Aboozar Taherkhani, Ammar Belatreche, Yuhua Li, Georgina Cosma, Liam P. Maguire, and T.M. McGinnity. A review of learning in biologically plausible spiking neural networks. *Neural Networks*, 122:253–272, 2020. ISSN 0893-6080. doi: https://doi.org/10.1016/j.neunet.2019.09.036. URL `https://www.sciencedirect.com/science/article/pii/S0893608019303181`.

Xiangwen Wang, Xianghong Lin, and Xiaochao Dang. Supervised learning in spiking neural networks: A review of algorithms and evaluations. *Neural Networks*, 125:258–280, 2020. ISSN 0893-6080. doi: https://doi.org/10.1016/j.neunet.2020.02.011. URL `https://www.sciencedirect.com/science/article/pii/S0893608020300563`.

Kashu Yamazaki, Viet-Khoa Vo-Ho, Darshan Bulsara, and Ngan Le. Spiking neural networks and their applications: A review. *Brain Sci*, 12(7), June 2022.

Qu Yang, Malu Zhang, Jibin Wu, Kay Chen Tan, and Haizhou Li. Lc-ttfs: Towards lossless network conversion for spiking neural networks with ttfs coding, 2023. URL `https://arxiv.org/abs/2310.14978`.

A APPENDIX

A.1 PROOFS OF EQUATIONS

Proof of Eq. (8) (A similar derivation leads to Eq. (5))

$$u_i^l[T] = \sum_j w_{ij}^l \sum_{t=1}^{T} \beta^{T-t} S_j^{l-1}[t] + \sum_{t=1}^{T} \beta^{T-t} b_i^l - \sum_{t=1}^{T} \beta^{T-t} S_i^l[t] \tag{A1}$$

Proof. Starting with the initial condition $u_i^l[0] = 0$ and Eq. (7), we can write:

$$u_i^l[1] = z_i^l[1] - S_i^l[1]$$

Next, we derive the expression for $u_i^l[2]$ by substitute the above into Eq. (7):

$$u_i^l[2] = \beta(z_i^l[1] - S_i^l[1]) + z_i^l[2] - S_i^l[2]$$

We can generalize this process to iteratively compute the membrane potential up to $t = T$:

$$u_i^l[T] = \sum_{t=1}^{T} \beta^{T-t}(z_i^l[t] - S_i^l[t])$$

substituting $z_i^l[t]$ from Eq. (4) and rearranging the terms, we get:

$$u_i^l[T] = \sum_{t=1}^{T} \beta^{T-t}(\sum_j w_{ij}^l S_j^{l-1}[t] + b_i^l - S_i^l[t])$$

Reorganizing the terms by summation yields:

$$u_i^l[T] = \sum_j w_{ij}^l \sum_{t=1}^{T} \beta^{T-t} S_j^{l-1}[t] + \sum_{t=1}^{T} \beta^{T-t} b_i^l - \sum_{t=1}^{T} \beta^{T-t} S_i^l[t]$$

□

A.2 PROOFS OF THEOREMS

Theorem 1. *Making $u_i^l[T] < \epsilon$ is equivalent to satisfying the following equation:*

$$\begin{aligned} &\forall t_0 \in \{1, 2, \cdots, T\}, \\ &\beta^{T-t_0+1} u_i^l[t_0 - 1] + \sum_j w_{ij}^l \sum_{t=t_0}^{T} \beta^{T-t} S_j^{l-1}[t] + \sum_{t=t_0}^{T} \beta^{T-t} b_i^l < \epsilon + \sum_{t=t_0}^{T} \theta^l \beta^{T-t} \end{aligned} \tag{A2}$$

Proof. We first prove the forward direction. Given that $u_i^l[T] < \epsilon$, we can express it using Eq. (7) and Eq. (4) as follows:

$$\beta u_i^l[T-1] + \sum_j w_{ij}^l S_j^{l-1}[T] + b_i^l < \epsilon + \theta^l \tag{A3}$$

Continue the above process, and we have:

$$\beta^2 u_i^l[T-2] + \sum_j w_{ij}^l \beta S_j^{l-1}[T-1] + \beta b_i^l + \sum_j w_{ij}^l S_j^{l-1}[T] + b_i^l < \epsilon + \theta^l + \beta\theta^l \tag{A4}$$

The above process can be repeated until we obtain an equation involving $u_i^l[0]$. The left-hand side of each equation regarding $u_i^l[t]$, where $t \in \{1, 2, \cdots, T\}$, can be organized to demonstrate that the forward reasoning is valid.

Then we proceed to prove the backward direction. For any $t_0 \in \{1, 2, \cdots, T\}$, by iteratively updating the membrane potential using Eq. (7) from $t = t_0$ until $t = T$, and substitute $z_i^l[t]$ with Eq. (4), we can get:

$$u_i^l[T] = \beta^{T-t_0+1} u_i^l[t_0 - 1] + \sum_j \sum_{t=t_0}^{T} w_{ij}^l \beta^{T-t} S_j^{l-1}[t] + \sum_{t=t_0}^{T} \beta^{T-t} b_i^l - \sum_{t=t_0}^{T} \beta^{T-t} S_i^l[t] \tag{A5}$$

Note that $\sum_t \beta^{T-t} S_i^l[t] \leq \sum_t \theta^l \beta^{T-t}$. Then we can write:

$$\begin{aligned} u_i^l[T] &\leq \beta^{T-t_0+1} u_i^l[t_0 - 1] + \sum_j w_{ij}^l \sum_{t=t_0}^{T} \beta^{T-t} S_j^{l-1}[t] + \sum_{t=t_0}^{T} \beta^{T-t} b_i^l - \sum_{t=t_0}^{T} \theta^l \beta^{T-t} \\ &< \epsilon \end{aligned} \tag{A6}$$

□

Theorem 2. *Let $S_j^{l-1}[t] \sim a_j^{l-1}$, $w_{ij}^l = \hat{w}_{ij}^l$, and $b_i^l = {}^{\hat{b}_i^l}/_{\sum_t \beta^{T-t}}$. Then $S_i^l[t] \sim a_i^l$, provided that $\left|u_i^l[T]\right| < \theta^l$.*

Proof. Eq. (8) can be organized into the following form:

$$\sum_{t=1}^{T} \beta^{T-t} S_i^l[t] = \sum_j w_{ij}^l \sum_{t=1}^{T} \beta^{T-t} S_j^{l-1}[t] + \sum_{t=1}^{T} \beta^{T-t} b_i^l - u_i^l[T] \tag{A7}$$

Given that $S_j^{l-1}[t] \sim a_j^{l-1}$, we use σ_j^{l-1} to denote the difference between the encoded value and the activation, defined as $\sigma_j^{l-1} = \sum_t \beta^{T-t} S_j^{l-1}[t] - a_j^{l-1}$. Substituting a_j^{l-1} and σ_i^l into Eq. (A7), we can write:

$$\begin{aligned} \sum_{t=1}^{T} \beta^{T-t} S_i^l[t] &= \sum_j w_{ij}(a_j^{l-1} + \sigma_j^{l-1}) + \sum_{t=1}^{T} \beta^{T-t} b_i^l - u_i^l[T] \\ &= \sum_j \hat{w}_{ij}(a_j^{l-1} + \sigma_j^{l-1}) + \hat{b}_i^l - u_i^l[T] \\ &= \sum_j \hat{w}_{ij} a_j^{l-1} + \hat{b}_i^l - u_i^l[T] + \sum_j \hat{w}_{ij} \sigma_j^{l-1} \end{aligned} \tag{A8}$$

According to Definition 1, we have $-\theta^l < \sigma_j^{l-1} < \theta^l$. Considering that θ^l is typically kept small to provide fine-grained encoding and $\hat{w}_{ij}$ is generally symmetrically distributed around zero, we can ignore the last term on the right-hand side of the equation. Since $S_i^l[T]$ can encode negative values, we implemented a ReLU counterpart to zero out these spike sequences, corresponding to the $\max(\cdot, 0)$ operation in Eq. (6). Combining Eq. (A8) with the condition $\left|u_i^l(T)\right| < \theta^l$ and Definition 1, we can conclude that $S_i^l[t] \sim a_i^l$. □

Theorem 3. *Let the input pixel value be a_i^0 and $\beta \leq 2$. By Initializing the membrane potential $u_i^0[0]$ with ${}^{a_i^0}/_{\beta^T}$, the resulting spike train $S_i^0[t] \sim a_i^0$ with T steps.*

Proof. We proof this theorem by mathematical induction. Let $\tilde{a}_{i.T}^0$ and m_T^0 denote the encoded value and the maximum encodable value, respectively, i.e. $\tilde{a}_{i,T}^0 = \sum_t \beta^{T-t} S_i^0[t]$, $m_T^0 = \sum_t \theta^0 \beta^{T-t}$.

step 1. For $T = 1$, it's obvious that:

$$\begin{cases} \left|\tilde{a}_{i,0}^0 - a_i^0\right| < \theta^0 & , a_i^0 < m_0^0 \\ \tilde{a}_{i,0}^0 = m_0^0 & , a_i^0 \geq m_0^0 \end{cases} \tag{A9}$$

step 2. Assume the statement is true for $T = t_0$, i.e. we have:

$$\begin{cases} \left|\tilde{a}_{i,t_0}^0 - a_i^0\right| < \theta^0 & , a_i^0 < m_{t_0}^0 \\ \tilde{a}_{i,t_0}^0 = m_{t_0}^0 & , a_i^0 \geq m_{t_0}^0 \end{cases} \tag{A10}$$

Note the relationship between θ^0 and $m^0_{t_0}$: $\theta^0 = \frac{m^0_{t_0}}{1+\beta+\cdots+\beta^{t_0-1}}$. Then we prove that for $T = t_0 + 1$, Eq. (A10) still holds.

case (1). For $a_i^0 < m^0_{t_0+1}$: Consider the first t_0 steps. It can be observed that this process is equivalent to encoding ${}^{a_i^0}\!/\beta$ with $m^0_{t_0} = \frac{1+\beta+\cdots+\beta^{t_0-1}}{1+\beta+\cdots+\beta^{t_0}} m^0_{t_0+1}$. Then we have:

$$\begin{cases} \left| \tilde{a}^0_{i,t_0} - \dfrac{a_i^0}{\beta} \right| < \dfrac{m^0_{t_0+1}}{1+\beta+\cdots+\beta^{t_0}} & , \dfrac{a_i^0}{\beta} < m^0_{t_0} \\ \tilde{a}^0_{i,t_0} = m^0_{t_0} & , \dfrac{a_i^0}{\beta} \geq m^0_{t_0} \end{cases} \tag{A11}$$

For $\frac{a_i^0}{\beta} < m^0_{t_0}$, we can write:

$$\beta \left| \tilde{a}^0_{i,t_0} - \frac{a_i^0}{\beta} \right| < \frac{\beta m^0_{t_0+1}}{1+\beta+\cdots+\beta^{t_0}} < \frac{2 m^0_{t_0+1}}{1+\beta+\cdots+\beta^{t_0}} = 2\theta^0 \tag{A12}$$

For $\frac{a_i^0}{\beta} \geq m^0_{t_0}$:

$$\begin{aligned} \beta \left| \tilde{a}^0_{i,t_0} - \frac{a_i^0}{\beta} \right| &= a_i^0 - \frac{1+\beta+\cdots+\beta^{t_0-1}}{1+\beta+\cdots+\beta^{t_0}} m^0_{t_0+1} \\ &\leq m^0_{t_0+1} - m^0_{t_0+1} \frac{1+\beta+\cdots+\beta^{t_0-1}}{1+\beta+\cdots+\beta^{t_0}} = \theta^0 \end{aligned} \tag{A13}$$

According to Theorem 1, $\beta \left| \tilde{a}^0_{i,t_0} - \frac{a_i^0}{\beta} \right| < 2\theta^0$ is equivalent to $\left| u_i^0[t_0+1] \right| < \theta^0$ (as there's neither input nor bias term). Also note $\left| u_i^0[t_0+1] \right| = \left| \tilde{a}^0_{i,t_0+1} - a_i^0 \right|$. Then we have $\left| \tilde{a}^0_{i,t_0+1} - a_i^0 \right| < \theta^0$.

case (2). For $a_i^0 \geq m^0_{t_0+1}$:

$$\frac{a_i^0}{\beta} \geq \frac{1}{\beta} m^0_{t_0+1} > \frac{1+\beta+\cdots+\beta^{t_0-1}}{1+\beta+\cdots+\beta^{t_0}} m^0_{t_0+1} = m^0_{t_0} \tag{A14}$$

Then we have:

$$\beta \left| \tilde{a}^0_{i,t_0} - \frac{a_i^0}{\beta} \right| = a_i^0 - \beta \frac{1+\beta+\cdots+\beta^{t_0-1}}{1+\beta+\cdots+\beta^{t_0}} m^0_{t_0+1} \geq \frac{m^0_{t_0+1}}{1+\beta+\cdots+\beta^{t_0}} = \theta^0 \tag{A15}$$

which means the neuron will fire a spike at $t = t_0 + 1$, leading to $\tilde{a}^0_{i,t_0+1} = m^0_{t_0+1}$. Combining case (1) and (2), and we have:

$$\begin{cases} \left| \tilde{a}^0_{i,t_0+1} - a_i^0 \right| < \theta^0 & , a_i^0 < m^0_{t_0+1} \\ \tilde{a}^0_{i,t_0+1} = m^0_{t_0+1} & , a_i^0 \geq m^0_{t_0+1} \end{cases} \tag{A16}$$

step 3. By the principle of mathematical induction, $\forall T \in \mathbb{N}^\star$:

$$\begin{cases} \left| \tilde{a}^0_{i,T} - a_i^0 \right| < \theta^0 & , a_i^0 < m^0_T \\ \tilde{a}^0_{i,T} = m^0_T & , a_i^0 \geq m^0_T \end{cases} \tag{A17}$$

Considering our initialization strategy for $\tilde{\theta}^0$ and subsequent data-based amplification, we can always ensure that $a_i^0 < m^0_T$. Thus, $\left| \tilde{a}^0_{i,T} - a_i^0 \right| < \theta^0$, which means $S_i^0[t] \sim a_i^0$. □

A.3 SPIKE AMPLITUDE ADJUSTMENT

Eq. (9) suggests that increasing θ^l can relax the constraints on the input. Let $\tilde{\theta}^l$ denote the initial spike amplitude. After getting the initialized value, we use a subset of the training set to perform forward propagation for the CSS-based SNN, and then calculate the 99.9th percentile u^l of the distribution of $u_i^l[T]$ for each layer l. If u^l exceeds θ^l, we amplify θ^l by a factor s^l. Note that increasing θ^l raises the firing threshold at the same time, making the change in $u_i^l[T]$ a complex nonlinear process. To determine a suitable s^l, we simplify the problem by assuming that $u_i^l[T]$

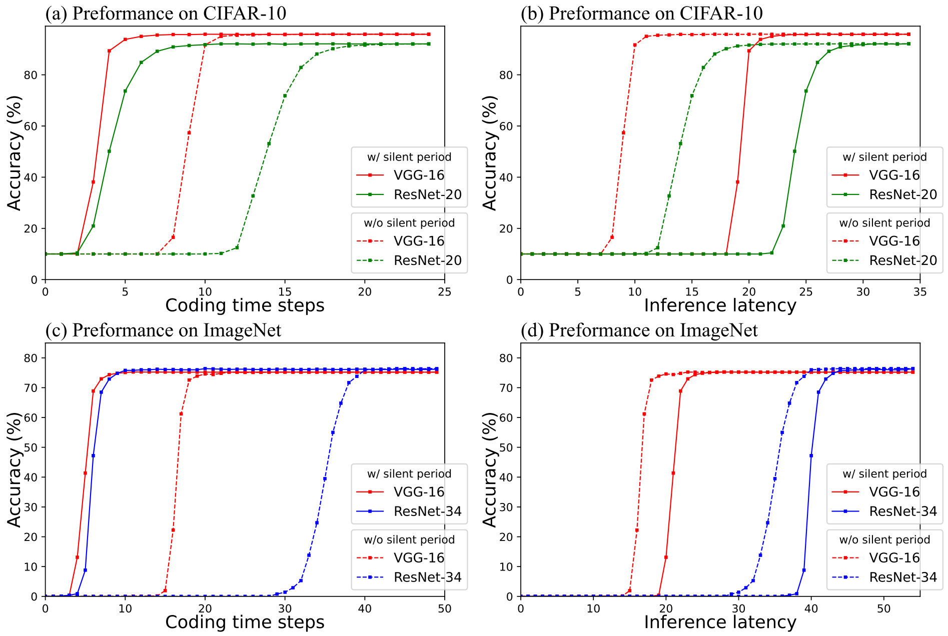
(a) Preformance on CIFAR-10

(b) Preformance on CIFAR-10

(c) Preformance on ImageNet

(d) Preformance on ImageNet

Figure 5: Trade-off between the coding time steps and inference latency. The dashed line represents the results obtained without the silent period, while the solid line represents the results achieved after incorporating the silent period. (a) Coding time steps on CIFAR-10. (b) Inference latency on CIFAR-10. (c) Coding time steps on ImageNet. (d) Inference latency on ImageNet.

accumulates uniformly over time. Thus, if the increment of θ^l is $\Delta\theta^l$, then $u_i^l[T]$ will decrease by $\Delta\theta^l \sum_t \beta^{T-t}$. Accordingly, s^l is determined using the following equation:

$$s^l = 1 + \begin{cases} \dfrac{u^l - \theta^l}{\sum_t \beta^{T-t}} & , u^l - \theta^l > 0.05 \cdot \displaystyle\sum_t \beta^{T-t} \\ \dfrac{u^l - \theta^l - 0.01 \cdot \sum_t \beta^{T-t}}{\sum_t \beta^{T-t}} + 0.04 & , 0.05 \cdot \displaystyle\sum_t \beta^{T-t} \geq u^l - \theta^l > 0.01 \cdot \displaystyle\sum_t \beta^{T-t} \\ \dfrac{4 \cdot (u^l - \theta^l)}{\sum_t \beta^{T-t}} & , 0.01 \cdot \displaystyle\sum_t \beta^{T-t} \geq u^l - \theta^l > 0 \end{cases} \tag{A18}$$

To ensure that the spike amplitude can still be effectively adjusted when u^l slightly exceeds θ^l, we increase the value of s^l for this range.

Note that an increase in θ^l makes the decoupling conditions for layer $l+1$ harder to meet[4]. Consequently, in deeper layers, the initial spike amplitude must be amplified by a large factor. This requires a sufficiently small $\tilde{\theta}^l$ to preserve adequate encoding granularity after scaling, which in turn necessitates a larger number of time steps. We address this issue by delaying the TSA output, which eliminates the need for $\tilde{\theta}^l$ amplification.

It is important to note that this adjustment lacks strict mathematical support and serves as a heuristic for fine-tuning the spike amplitude. The introduction of negative spikes remains the core mechanism for breaking temporal coupling.

A.4 CODING TIME STEPS VS. INFERENCE LATENCY

According to the analysis in Appendix A.3, relying solely on θ^l amplification to break temporal coupling would require smaller $\tilde{\theta}^l$ in deeper layers, which leads to an increase in coding time steps. To address this, we introduce a one-step silent period to achieve a trade-off between coding time steps

---

[4] In Eq. (9), the spike amplitude of the previous layer is included in $S_j^{l-1}[t]$.

and inference latency. In this section, we conducted an ablation study to assess the effectiveness of this approach. We performed classification tasks on CIFAR-10 using VGG-16 and ResNet-20, and on ImageNet using VGG-16 and ResNet-34. Fig. 5 (a) and (c) present the relationship between coding time steps and accuracy, while Fig. 5 (b) and (d) show the relationship between inference latency and accuracy.

The experimental results indicate that even with no silent period, deeper networks experience larger latency due to increased coding time steps. This can also be understood as neurons in each layer require time to accumulate membrane potential before firing. Thus, incorporating a silent period has a limited effect on increasing inference latency, but plays a significant role in reducing coding time steps. For example, in ResNet-20 on CIFAR-10, the silent period increased latency from 20 to 30 steps but halved the coding time steps, greatly improving throughput. This effect becomes more pronounced with increased network depth or dataset scale. For instance, with ResNet-34 on ImageNet, the silent period added only about 5 steps to inference latency while reducing coding time steps by approximately 30 steps. Overall, incorporating the silent period effectively reduces the required number of time steps for encoding, substantially improving throughput with minimal impact on latency.

It is important to note that although the requirement ofTheorem 2 can be satisfied by amplitude adjustment on training set, this does not ensure optimal performance on the test set. By contrast, silent period provides a data-independent approach to break temporal coupling, resulting in more stable and consistent performance improvements.

A.5 MATHEMATICAL DESCRIPTION OF THE TSA NEURON

To generalize the representation, let T_s denote the length of the silent period. For a TSA neuron in the l-th layer, when the time step $t \in \{1, 2, \ldots, T_s l\}$, the membrane potential remains $u_i^l[t] = u_i^l[0] = 0$, and no spikes are generated. After this period, the neuron processes inputs in cycles of length $T + T_s$. Let T_a^k denote the start of the k-th cycle, i.e. $T_a^k = T_s l + k(T_s + T) + 1$, and let T_b^k denote the end of the cycle, i.e. $T_b^k = T_s l + (k+1)(T_s + T)$, with k being a natural number. Without loss of generality, we consider the case where $t \in \{T_a^k, T_a^k + 1, \ldots, T_b^k\}$.

The set of its spike times can be expressed as follows:

$$\mathbb{F}_i^l = \left\{ t_i^{l,f} \,\middle|\, \left| o_i^l[t_i^{l,f}] \right| \geq \frac{\theta^l \beta^{T_s}}{2},\ t_i^{l,f} \in \{T_a^k + T_s, T_a^k + T_s + 1, \cdots, T_b^k\} \right\} \tag{A19}$$

The spike sequence it emits, $S_i^l[t]$, can then be written as:

$$S_i^l[t] = \sum_{t_i^{l,f} \in \mathbb{F}_i^l} \operatorname{sgn}\left(o_i^l[t_i^{l,f}] \right) \theta^l \delta[t - t_i^{l,f}] \tag{A20}$$

where $\delta[\cdot]$ denotes an unit impulse, $\operatorname{sgn}(\cdot)$ is the sign function and θ^l is the spike amplitude. The update process of the membrane potential can be expressed as follows:

$$u_i^l[t] = \beta u_i^l[t-1] + z_i^l[t] - \beta^{T_s} S_i^l[t] \tag{A21}$$

where $z_i^l[t]$ denotes the integrated inputs:

$$z_i^l[t] = \sum_j w_{ij}^l S_j^{l-1}[t] + b_i^l \tag{A22}$$

A.6 PSEUDO CODE FOR CONVERSION PROCESS

See Algorithm 2. The spike amplitude for each layer is determined using the method outlined in Section 4.2.1. Note that this value is absorbed into the weights and bias, so after conversion, the spike amplitudes for TSA neurons are all normalized to 1. For data-based spike amplitude adjustment, we first complete the above conversion process using the initial spike amplitudes. Then, based on the residual membrane potentials observed in the resulting SNN, we update the spike amplitudes. These updated values are then used to re-convert the ANN. The process can be repeated as may times as needed.

Algorithm 2: Algorithm for ANN-SNN conversion

```
Input: ANN model $f_A(\hat{\boldsymbol{W}}, \hat{\boldsymbol{b}})$, encode time steps $T$, amplification factor $\beta$, spike amplitude $\theta^l$
       for each layer $l$, total layer number $L$
Output: SNN models $f_S(\boldsymbol{W}, \boldsymbol{b})$
reshape and pad $X$ to [T, B, C, H, W] with zeros to shape [(T+L), B, C, H, W];
membrane potential $M \leftarrow$ zeros_like $(X[0])$, threshold $v \leftarrow \frac{1}{2}\theta\beta^L$;
set CSS encoder for the input layer;                      /* see Theorem 3 */
for $1 \le l \le L$ do
    $W^l \leftarrow \frac{\theta^{l-1}}{\theta^l}\hat{W}^l$;                             /* norms $\theta^l$ in SNN to 1 */
    $b^l \leftarrow \frac{1}{\sum_{t=0}^{T-1}\beta^t\theta^l}\hat{b}^l$;
    replace ReLU activation with TSA and ReLU counterpart.
end
```

A.7 IMPLEMENTATION OF THE RELU COUNTERPART

In the actual implementation, we fuse the ReLU counterpart into the TSA neuron model to speed up program execution. We refer to this model as TSA-ReLU neuron. Below, we continue the notation from Appendix A.5 to present the mathematical model of TSA-ReLU. Without loss of generality, we consider the case where $t \in \{T_a^k, T_a^k + 1, \dots, T_b^k\}$. We use $h_i^l[t]$ and $g_i^l[t]$ to represent the accumulated input and output of TSA-ReLU, respectively:

$$\begin{aligned} h_i^l[t] &= \sum_j w_{ij}^l \sum_{\tau=T_a^k}^{t} \beta^{t-\tau} S_j^{l-1}[\tau] + \sum_{\tau=T_a^k}^{\max(t, T_a^k+T)} \beta^{t-\tau} b_i^l \\ g_i^l[t] &= \sum_{\tau=\min(T_a^k+T_s, t)}^{t} \beta^{t-\tau} S_i^l[\tau] \end{aligned} \tag{A23}$$

Then we set $o_i^l[t]$ according to the following equation:

$$o_i^l[t] = \begin{cases} h_i^l[t] - g_i^l[t] & , h_i^l[t] \ge 0, t \ge T_a^k + T_s \\ -g_i^l[t] & , h_i^l[t] < 0, t \ge T_a^k + T_s \\ 0 & , t < T_a^k + T_s \end{cases} \tag{A24}$$

The firing condition of TSA-ReLU is the same as that of TSA, and is given by Eqs. (A19) and (A20).